A novel technique for time-resolved detection and tracking of interfacial and matrix fracture in layered materials

Karel Minnaar[1], Min Zhou[*]

The George W. Woodruff School of Mechanical Engineering, Georgia Institute of Technology, 801 Ferst Drive, Atlanta, GA 30332-0405, USA

Abstract

A novel experimental technique is developed for time-resolved detection and tracking of damage in the forms of delamination and matrix cracking in layered materials such as composite laminates. The technique is non-contact in nature and uses dual or quadruple laser interferometers for high temporal resolution. Simultaneous measurements of differential displacement and velocity at individual locations are obtained to analyze the initiation and progression of interfacial fracture and/or matrix cracking/delamination in a polymer matrix composite laminate system reinforced by graphite fibers. The measurements at multiple locations allow the speeds at which interfacial crack front (mode-I) or matrix cracking/delamination front (mode-II dominated) propagates to be determined. Experiments carried out use three-point bend configurations. Impact loading is achieved using a modified Kolsky bar apparatus with a complete set of diagnostics for load, deformation, deformation rate, and input energy measurement. This technique is used to characterize the full process of damage initiation and growth. The experiments also focused on the quantification of the speed at which delamination or damage propagates under primarily mode-I and mode-II conditions. The results show that the speed of delamination (mode-I) or the speed of matrix cracking/delamination (primarily mode-II) increases linearly with impact velocity. Furthermore, speeds of matrix failure/delamination under primarily mode-II conditions are much higher than the speeds of mode-I crack induced delamination under mode-I conditions.
© 2004 Elsevier Ltd. All rights reserved.

Keywords: Interfacial fracture; Delamination; Matrix cracking; Layered materials; Time-resolved tracking; Laser interferometry; Crack speed

[*] Corresponding author. Tel.: +1-404-894-3294; fax: +1-404-894-0186.
E-mail address: min.zhou@me.gatech.edu (M. Zhou).

[1] Currently at ExxonMobil Upstream Research Company, Houston, TX.

1. Introduction

Damage in layered materials such as composite laminates has been extensively studied over the past 20 years. Initial studies considered damage under quasi-static conditions and revealed the basic mechanical processes of damage initiation and growth. One area of interest is foreign body impact on composite laminates. The mechanisms for damage due to low velocity impact include matrix-cracking, fiber breakage and delamination (Abrate, 1991, 1994, 1998). Delamination is by far the most important of these mechanisms since it causes the greatest reduction in strength. Delamination is a concern to the aircraft industry. For example, delamination can be caused by in-service impact events such as tools dropping on structures, hail falling on surfaces, collision with birds, and rocks or debris being kicked up at high velocities into aircraft. Since layered composite materials are extensively used in modern aircraft, a design methodology to improve damage tolerance has been sought. A study concerning aircraft wing panels was conducted by Wiggenraad et al. (1999). They analyzed impact damage to heavily loaded, blade-stiffened composite wing panels and found that delamination can lead to global bending, instability and collapse. Delamination damage caused by dropped tools is difficult or impossible to detect visually, but will grow during subsequent compressive loading. It is important to understand how delamination initiates and grows in a structure in order to prevent catastrophic failure caused by the reduction in strength of the layered component.

Transverse shear stress is the primary cause for damage in layered composite structures under conditions of low-velocity impact (Joshi and Sun, 1986). Delamination and matrix-cracking have been found to be the major damage modes (Joshi and Sun, 1985) and the damage behavior of composite structures is significantly influenced by matrix material, stacking sequence, and specimen thickness (Cantwell and Morton, 1991). It is known that the property mismatch in layered composite materials is one cause for delamination (Agarwal and Broutman, 1990). Test results have shown that upon impact a laminated composite panel can suffer a significant loss of its design strength without visible indication of damage on the impacted surface. Once delamination begins, it can influence the fatigue behavior of the material and can initiate crack branching or intra-layer cracking in the transverse plies (La Saponara and Kardomateas, 2000; Pelegri and Kardomateas, 1998).

1.1. Initiation and propagation of interlaminar delamination

Experiments have shown that a threshold velocity exists below which no delamination is detected (Davies et al., 2000). Above this threshold, damage may appear limited as impact indentations on the surface. However, significant internal damage may be present in the forms of matrix-cracks and interlayer delamination. Early studies focused on the effect of impactor shape and delamination area in glass epoxy composites (Cristescu et al., 1975). Delamination only occurs between layers with different orientations (Dost et al., 1991). Investigators have studied the shape of delamination zones (Joshi and Sun, 1985; Joshi and Sun, 1986). Takeda et al. (1982) reported

matrix-cracks in the presence of delamination. They described the average spacing of matrix-cracks in the damage zone created during impact.

Chang and coworkers (Chang et al., 1989, 1990a,b; Chang and Lessard, 1991; Choi et al., 1990, 1991a,b) completed extensive experimental and numerical studies of impact-induced damage. They used a gas gun to apply loading on laminated composites with a line impactor. The material studied is a carbon fiber/epoxy reinforced system. Various cross-ply lay-up schemes are considered. They showed that in-ply matrix-cracks are the initial damage mode. Shear and bending matrix-cracks are also identified. The shear cracks appear inside the laminate and are located away from the impacted area and grow at an angle to the ply interface. Delamination initiates once the matrix-cracks have propagated to the interfaces between plies with different orientations. These matrix-cracks are referred to as "critical matrix-cracks". A shear matrix crack can cause a substantial amount of delamination along the bottom interface away from the impacted area and a small confined delamination along the upper interface towards the impacted area. In the case of a shear matrix crack in a 90° layer, delamination is initiated in mode I and the subsequent propagation of delamination is primarily mode-II. This failure mechanism is confirmed by Salpekar (1993) who showed that a significant mode-I component of the strain energy release rate is present at delamination initiation. Others also studied the mode of propagation for delamination (Choi et al., 1991b; Grady and Sun, 1986; Liu et al., 1993; Sun and Manoharan, 1989; Tao and Sun, 1997). These studies clarified the mode of delamination propagation under different loading conditions.

1.2. Time-resolved detection of delamination and damage

Even though the mechanisms responsible for delamination are understood, it is important to characterize the conditions under which interfacial and matrix fracture initiates and propagates. Quantification of the effects of loading conditions and loading mode is especially lacking. Most experiments have focused on the examination of damage after impact loading or on the characterization of the post-impact behavior of materials. Analyses of the influence of fiber properties, matrix properties, interphase properties and fiber stacking sequence are primarily based on post-impact observations. These postmortem analyses essentially use a snapshot at the end of the damage progress to assess material behavior and response. Time-resolved assessment of damage progression during loading is important for understanding the behavior of layered materials. There is a strong need for useful tools and techniques that allow detection and analysis of the initiation and growth of delamination. The following techniques allow for a degree of in situ or time-resolved monitoring of damage progression:

The load history and delamination load threshold (*DLT*) *method*: The impact force history has often been used to interpret damage (Cartie and Irving, 2002; Lagace and Wolf, 1993; Schoeppner and Abrate, 2000; Strait et al., 1992). The maximum force preceding a rapid decrease in the force profile is often called the threshold force (P_c). This value and the time at which it occurs are often associated with initiation of damage in the forms of matrix-cracking, fiber breakage and delamination. Davies and Zhang (1995) and Davies et al. (2000) related the threshold force to the mode-II delamination

toughness in a quasi-isotropic laminate as

$$P_c = \frac{8\pi^2 Eh^3}{9(1-v^2)} G_{IIC},$$ (1)

where G_{IIC} is the mode-II interlaminar critical energy release rate, E is the equivalent Young's modulus, v is the equivalent Poisson's ratio and h is the thickness of the material. Cartie and Irving (2002) showed that this relation holds true for a number of commercially available carbon/epoxy composite laminates. It must be noted that the maximum load provides only an approximate indication for rapid development of damage. Minnaar and Zhou (2004) have shown that it does not provide an accurate indication of the initiation of damage.

High-speed photography: High-speed photography has been employed by some to determine the onset and propagation speed of interfacial cracks. Takeda et al. (1982) used a back-light photographic technique to record the positions of a delamination front in translucent materials. They reported delamination speeds on the order of 200–500 ms^{-1}. Chai et al. (1983) used a high-speed camera coupled with a shadow-Moire technique to measure delamination propagation in a composite panel. Hallett (2000) used a modified Kolsky (split Hopkinson) bar apparatus and high-speed photography to correlate the failure of impacted beams to abrupt changes in measured deflection.

Acoustic emission and electric resistance method: Acoustic emission techniques have been combined with microscopic observations to obtain continuous monitoring of damage growth. Benmedakhene et al. (1999) used such a technique to study the effect of impact velocity on mode-I strain energy release rate. They are unable to precisely correlate the initiation of damage with acoustic emissions and had to revert to surface mounted strain gauges to determine the initiation of through thickness cracks. Abry et al. (1999, 2001) suggested that increases in electrical resistance during monotonic loading of carbon-fiber-reinforced polymers are indicative of fiber breakage. However, the technique has not been used under impact conditions nor has it been shown to apply to other damage modes. Todoroki et al. (2002) suggested that the delamination zone size and location can be inferred from a series of electrodes mounted on a specimen. Calculations are based on measured changes of resistance between two electrodes. However, determination of the location of crack front is challenging since the electric-resistance can change between two electrodes even when the crack is located far away from the electrodes. Also, the measurement was not made in real-time.

Surface mounted gauges: Tsai et al. (2001) and Guo and Sun (1998) measured crack speeds in a modified end-notched flexure specimen (ENF) by means of conductive aluminum lines deposited on the edge of the specimen. The conductive lines break as the crack front propagates, allowing the crack tip speed to be inferred. A very low loading rate of 0.025 (mm)s^{-1} was used to facilitate numerical calculations. However, they reported crack speeds in excess of 1000 ms^{-1}. They also experienced difficulties in measuring speeds under pure mode-II loading. It is unclear if this method would work under impact loading since an enamel layer has to be applied to the edge of the specimen to conductively insulate the deposited wires from the specimen. This layer could debond and crack during an impact event.

Full field laser interferometry: Lambros and Rosakis (1995) and Lambros and Rosakis (1997a) presented an advanced technique to obtain real-time full field visualization of crack growth in composite laminates. They used the Coherent Gradient Sensor (CGS) in conjunction with high-speed photography to obtain real-time interferograms of the out-of-plane deformation on a surface. The configuration involved transversely impacted quasi-isotropic laminates. They found that delamination growth appears to occur in bursts and that delamination speed increases with impact velocity. The experiment requires special preparation of the specimen surface. Interframe times are on the order of 100 μs. Huang et al. (1999) studied, analytically and experimentally, the mode-I and mode-II propagation of a single crack in a uni-directional composite. Using the CGS system, they showed that mode-I crack growth never exceeds the shear wave speed and that for mode-II propagation there exists a crack tip velocity higher than the shear wave speed at which the crack will propagate in a stable manner.

Inherent disadvantages exist in the above techniques. For example, surface-mounted gauges can perturb the process under consideration and may fail as the surface deforms. Techniques based on conductivity or acoustic emissions infer damage indirectly and can be sensitive to factors unrelated to damage. It is not always clear that the measurements are actually attributed to delamination, matrix-cracking, fiber breakage, or fiber/matrix debonding. The load history method does not distinguish the effects of different damage mechanisms. It only provides an approximate indication of rapid development of damage and cannot capture the condition of damage initiation.

2. Description of technique

In this paper, a novel experimental technique is described. The laser interferometer-based technique developed here provides a non-contact approach for the characterization of delamination and matrix cracking. It is valid for time-resolved analyses over the whole history of an experiment. It offers very high temporal resolutions of up to 0.1 μs and can easily be applied to and reconfigured for different loading conditions and specimen configurations. It is expected that this method will yield novel experimental data and allow new insight to be gained into the dynamic process of damage development in layered materials.

2.1. Material

The material used is a $[0°/90°/0°]$ layered composite laminate made from NCT-301-1G150 (50 K) graphite/epoxy impregnated tape, which is highly toughened and contains unidirectional carbon fiber reinforcements. The material parameters are listed in Table 1. The microstructure of the two-phase epoxy-matrix/carbon-fiber reinforced composite that forms each layer of the material is shown in Fig. 1. The fiber diameter is 5 μm. The average fiber volume is 50%. The local fiber volume can be as high as 62% in fiber-rich areas and as low as 40% in resin-rich areas.

Table 1
Material parameters for the NCT-301 carbon fiber reinforced epoxy analyzed

Parameter	Value
Tensile modulus E_{11}	113.9 GPa
Tensile modulus E_{22}	7.985 GPa
Tensile strength σ_{11}	1621 MPa
Tensile strength σ_{22}	48.28 MPa
Poisson ratio v_{12}	0.288
Poisson ratio v_{21}	0.02
Shear modulus G_{12}	3.137 GPa
Shear strength S	33.3 MPa
Density ρ	1480 kg/m^3
Dilatational wave speed parallel to fibers C_L''	8773 ms^{-1}
Dilatational wave speed perpendicular to fibers $C_L^\perp$	2323 ms^{-1}
Shear wave speed C_s	1560 ms^{-1}

2.2. Experimental configurations

Three-point bend loading is used to generate predominantly mode-I and mode-II loading conditions, allowing delamination behavior under the respective settings to be studied and characterized.

Fig. 2(a) shows a schematic illustration of the opening mode specimen which is a rectangular strip 150 mm × 18 mm in size and 3 mm in thickness. It is simply-supported at its two ends and is impacted at the center. A line-nosed impactor is used to ensure a uniformly distributed load across the width of the specimen. This uniform load produces uniform damage throughout the width of the specimen, simplifying the impact damage process to a two-dimensional event, Choi et al. (1991a). A 0.3 mm thick diamond-grinding wheel is used to cut a starter crack in the longitudinal ply of the composite beam. The 1 mm deep starter crack is located at the center and extends across the width of the beam. This pre-crack serves as the initiation site for a matrix crack and the subsequent delamination from the location where the matrix crack intersects the ply interfaces. Impact occurs at the center of the specimen on the side opposite to the starter crack. In the experiments conducted, $L = 9.03$, 11.71 or 14.95 mm. The distance between the two locations of measurement d, ranged between 2 and 5 mm.

Fig. 2(b) shows a schematic illustration of the shear matrix-crack (Mode-II) configuration. Again, the specimen is a rectangular strip 150 mm × 18 mm in size and 3 mm in thickness. The specimen is clamped at both ends and impacted at the center, causing shear matrix-cracks to form in the transverse ply. Delamination initiates at the points where the matrix-cracks reach the ply interfaces. Delamination grows towards the impactor in the upper interface and away from the impactor in the lower interface. The interferometers are positioned such that the propagation of delamination in the lower interface (away from the impact side) is measured. The same L and d values as those in the configuration in Fig. 2(a) are used in this configuration as well.
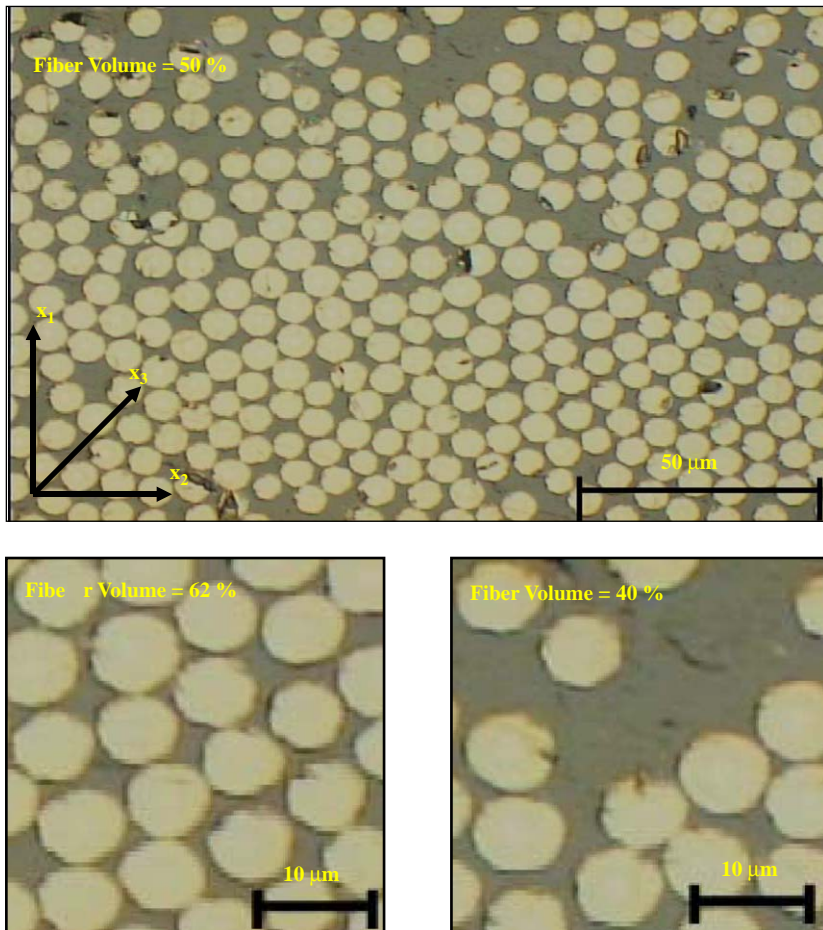
Fig. 1. Microstructure of the material analyzed.

In both configurations, the specimens are mounted on a rigid fixture. The fixture is adjustable, allowing specimens with different span lengths to be tested. Different impact velocities in the range of 3–8 ms^{-1} are used to delineate the effects of loading rate on the deformation and failure behavior of the material analyzed. The experiments are designed to allow analyses of the onset and progression of delamination due to transverse impact loading. The impact loading is achieved on a modified Kolsky or split Hopkinson bar apparatus, as illustrated in Fig. 3. The length of the striker bar used is 0.6 m. The shaped impactor is attached to a bar 1.5 m in length, giving rise to a loading pulse duration of 0.242 ms. A stopper is used in some experiments to ensure that only one loading pulse is applied to the specimens. High-speed digital oscilloscopes are used to record the signals from the strain gauges mounted on the incident bar and from the laser interferometers with a time resolution of 0.1 μs. The
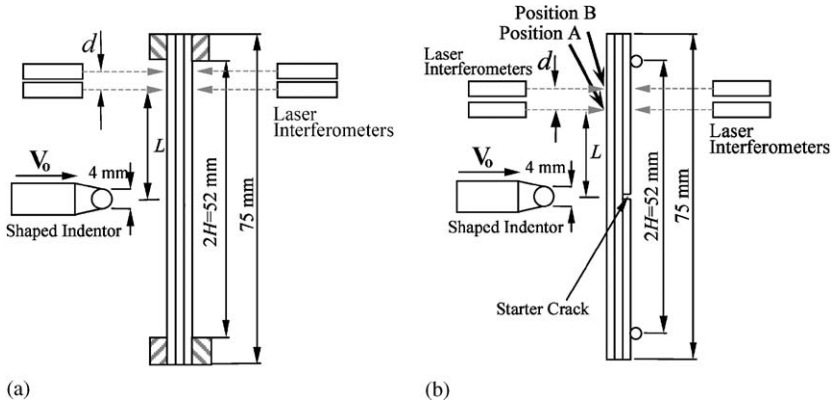
Fig. 2. Experiments for non-contact detection of interfacial fracture: (a) center-crack (primarily mode-I) configuration, (b) shear-crack (primarily mode-II) configuration.
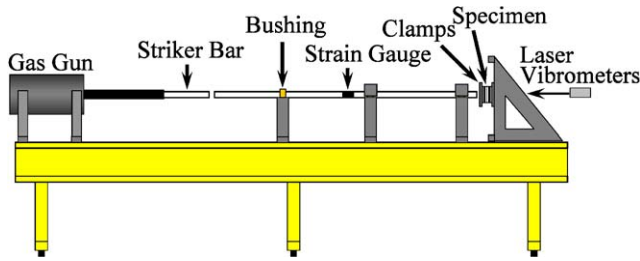

Fig. 3. Modified Kolsky bar apparatus for dynamic loading and time-resolved interfacial fracture analyses.

strain gauge signals are used to deduce histories of applied force, impact point velocity, impact point displacement, and input energy. The analysis of these quantities follows the technique developed by Park and Zhou (2000).

A pair of Polytec QFV-511 laser vibrometers is used for the simultaneous measurements of the displacements and velocities on the two sides of the specimen at each location (e.g., location A in Fig. 2). An array of interferometers are positioned at multiple locations along the specimen (e.g., locations A and B in Fig. 2) to capture the progression of delamination. The signals are used to obtain the time of onset of delamination at various locations away from the impact site. This novel capability is especially useful in directly measuring the speed at which delamination fronts propagate. In this research, four interferometers are used to capture the onset and propagation of delamination. The average speed of interfacial delamination between locations A and B along the span of the specimens is calculated using the measurements from the optical sensors.

An one-point configuration with two laser interferometers is used in the early stages of this study. Most experiments are carried out with measurements at two locations as

illustrated in Fig. 2. Each laser interferometer system consists of an optical fiber sensor head and an interferometric controller. The four OFV-511 interferometers are used with a combination of both standard OFV-102 fiber heads and side-exit probes to achieve precise positioning of the laser beams in the tight space around the specimen. Each controller contains two separate decoders, one for velocity measurement and the other for displacement measurement, allowing both the displacement and velocity associated with each beam to be recorded independently and simultaneously. The displacement and velocity decoders operate in different measurement ranges. For the experiments conducted, the velocity decoder is set to a full-range scale of ± 10 ms^{-1} with a resolution of 5.0 (μm)s^{-1} and has a maximum frequency of 1500 kHz. The displacement decoder is set to a full-range scale of 20.480 μm with a resolution of 4.8 μm and has a maximum frequency of 100 kHz.

In addition to the laser vibrometers and strain gauges, an IMACON 200 high-speed digital camera is used to record deformed shapes of the specimens during the experiments. The camera offers framing rates of up to 200 million frames per second. Each frame has a resolution of 1024×1280 pixels.

2.3. Measurement scheme

The detection and tracking of interfacial fracture use the fact that motions of the front surface (impact side) and the back surface of a specimen diverge upon interfacial separation. The primary objective of the experimental design is to obtain the differential displacement and differential velocity between the two sides through measurements of the respective surface displacements and velocities. Separate laser beams are used for each side. The lasers are aligned such that the two beams are coaxial and perpendicular to the specimen surfaces before impact. An optical scheme is used to achieve this alignment. This scheme involves the use of a cube beam splitter and the adjustment of beam locations and orientations in the absence of the specimen before the experiment. The alignment scheme is illustrated in Fig. 4. Specifically, the two laser beams enter opposite sides of the cube and are reflected at 90° to their respective incident paths. The reflected laser beams exit the cube from opposite sides. One side of the cube, where one of the reflected beams exits, is coated with a reflective layer so that beam is reflected back into the cube and is caused to exit the cube from the same side and in the same direction as the other beam. The two laser heads are then adjusted until the laser beams coincide at two or more locations, indicating coaxiality. The cube beam splitter is removed and the specimen is inserted into the setup after the alignment process. To ensure perpendicularity of the beams relative to the specimen surface, small pinholes are used to cause the reflected beams to return along the same paths as the incident beams. This involves the adjustment of specimen orientation until the reflected beams go through the same pinholes as the incident beams at distances away from the specimen. The specimen is fixed onto the rigid mount after all adjustments are made.

The interferometers measure both the velocities and displacements at the two points on the opposite surfaces of the specimen, in the direction perpendicular to the initial specimen surface. To understand how delamination is detected, consider the general
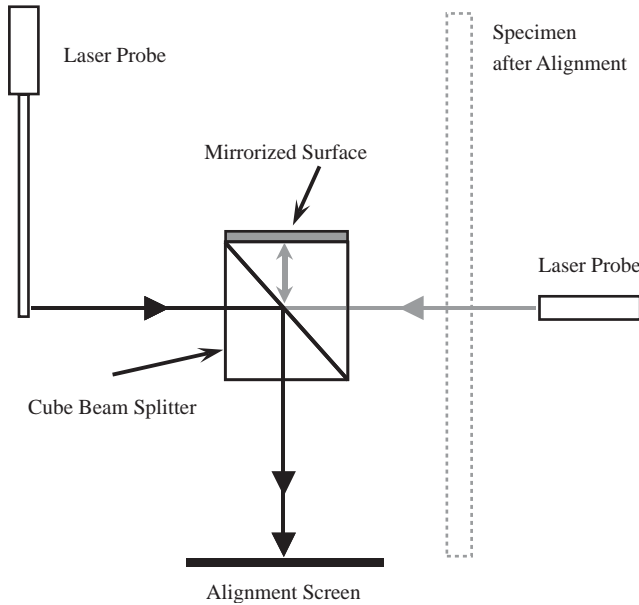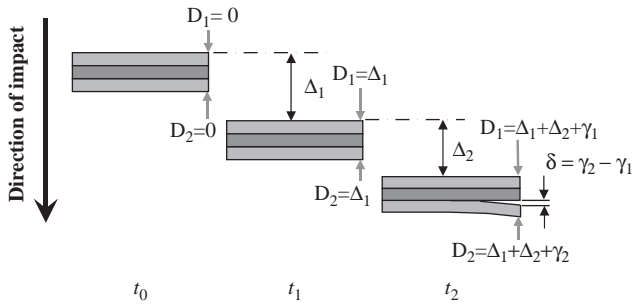
Fig. 4. Alignment of laser beams.

Fig. 5. Measurement of interfacial separation during specimen translation without rotation.

deformation of a specimen. Assume that the specimen behaves elastically except for the separation along the interface. Since dimensional changes associated with bulk deformation are extremely small, the specimen deformation can be regarded as a combination of the rigid bulk motion and interfacial separation due to fracture.

To facilitate discussion, consider the transverse motion of a specimen in the negative y-direction, as illustrated in Fig. 5. At t_0, the specimen is stationary and $D_2 = D_1 = 0$, where D_1 is the displacement of the impact side surface and D_2 is the displacement of the rear surface of the specimen, as measured by two interferometers. Displacements in the direction of impact are defined as positive for both interferometers. At t_1, the

specimen moves by an amount Δ_1 and both interferometers record the same displacement, i.e., $D_2 = D_1 = \Delta_1$. The interferometers also measure the same velocity, because the points move together during the rigid body motion of the specimen. Between t_1 and t_2, the specimen traverses an additional distance, Δ_2, and undergoes interfacial separation at the location of measurement. The points cease to move with the same displacement and velocity. Each interferometer measures an additional displacement due to delamination. Let γ_1 be the additional amount measured by the interferometer on the impact site and let γ_2 be the additional amount measured by the interferometer on the rear side due to delamination. Clearly,

$$\delta = D_2 - D_1 = \gamma_1 - \gamma_2 \tag{2}$$

is the difference between the measured displacements due to the separation at the layer interface. This differential displacement is a direct measure of the amount of separation at the point of measurement. Similarly, the corresponding differential velocity

$$\Delta V = V_2 - V_1 \tag{3}$$

is also a direct measure of the instantaneous rate of separation at the location of analysis. Both measures are equally valid and complement each other, with the differential velocity being a more sensitive indicator of interfacial fracture.

The above analysis does not consider the rotation of the specimen during deformation. This effect is illustrated in Fig. 6(a). Assume the angle of rotation is θ at the location of analysis. If γ_3 is the measurement by the interferometer on the impact site and γ_4 is the measurement by the interferometer on the rear side induced due to the rotation, the differential displacement due to the rotation is

$$\omega = \frac{h}{\cos\theta} - h = \gamma_4 - \gamma_3, \tag{4}$$

where, h is the thickness of the specimen. As illustrated in Fig. 6(b), an upper limit (conservative) estimate for θ for the configuration in Fig. 2 is

$$\theta(L') = \tan^{-1}\left(\frac{\Delta}{L'}\right) \approx \frac{\Delta}{L'}, \tag{5}$$

where, Δ is the average surface displacement measured by the interferometers and L' is the distance between the closer support and the measurement location. This estimate is conservative since it assumes that the deformed shape of the beam is bi-linear.

More accurate accounts of the effects of rotation can be obtained with estimates of the rotation angle using quasi-static solutions of the deflection curves for simply supported and clamped beams under a center load. The approximate rotations angles are, respectively,

$$\theta(L') = \frac{3(H^2 - L'^2)\Delta}{3H^2L' - L'^3} \tag{6}$$

for the opening crack configuration, and

$$\theta(L') = \frac{6(H - L')\Delta}{3HL' - 2L'^2} \tag{7}$$
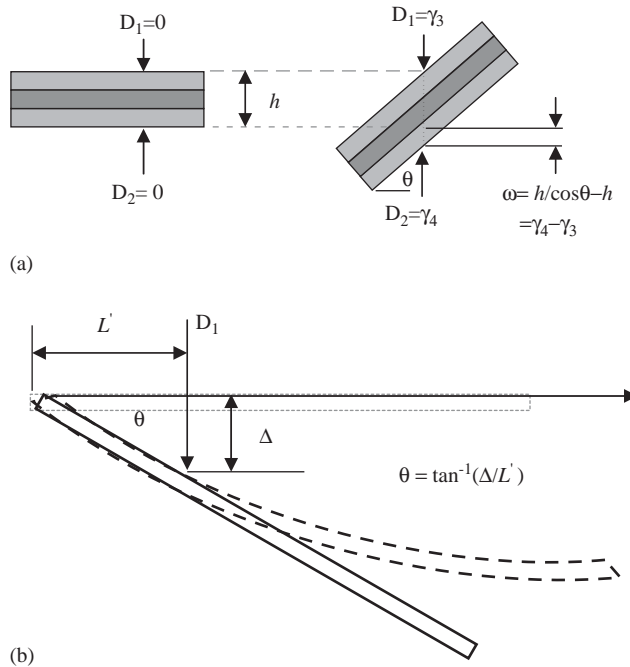
Fig. 6. Effect of rigid body rotation on measurement, (a) output due to rotation, (b) an upper bound estimate of the rotation angle.

for the shear crack configuration. H is the half span of the specimens as illustrated in Fig. 2. Corrections ω to the separation δ due to these rotations are to be calculated according to Eq. (4). It can be shown that the error ω is actually quite small under the conditions of the experiments carried out here. A specific estimate of the upper bound of the correction in an actual experiment will be given later in Section 3. In general, $\theta(L') \ll 1°$ at onset of fracture, giving rise to only very small errors.

3. Results

3.1. Detection and tracking of interfacial crack and damage propagation

To illustrate the application and sensitivity of the method developed here, the measured histories of surface displacements, differential displacement, and differential velocity from an experiment without delamination are shown in Fig. 7. The configuration in Fig. 2(a) with the opening mode specimen is used. The impact velocity is 2 ms^{-1} and no delamination or damage is observed in the specimen after the experiment. The two surface velocity profiles coincide. The differential displacement and differential velocity profiles remain close to zero throughout the experiment, consistent with what is expected for this experiment. The histories of input work, displacements, differential
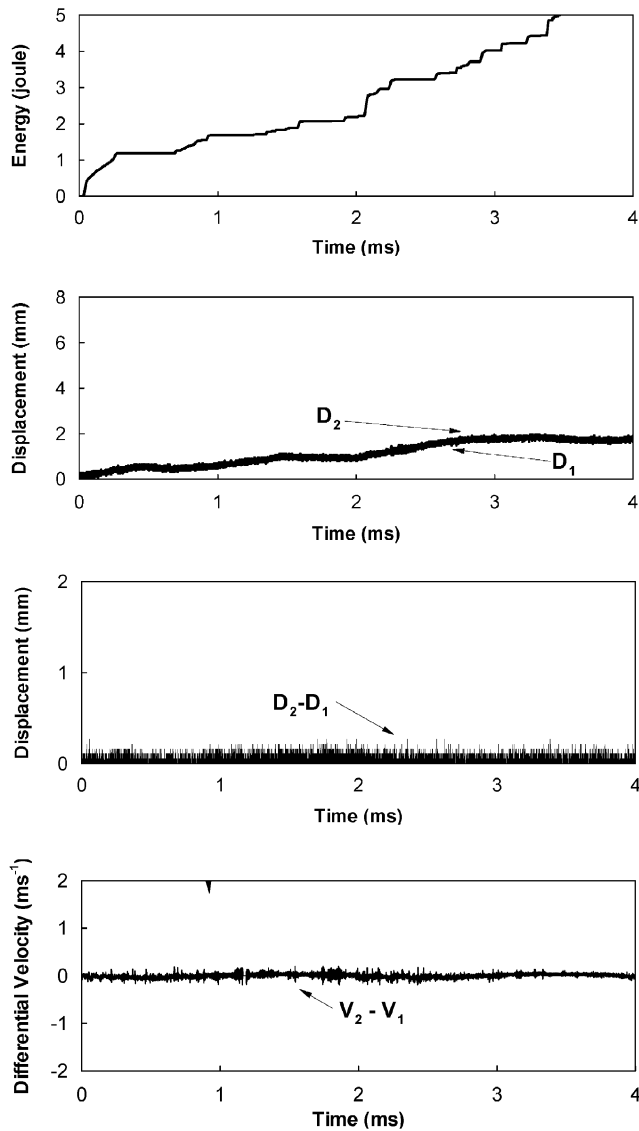
Fig. 7. Histories of displacements, differential displacement and differential velocity for a mode-I experiment without delamination ($V_0 = 2.0 \text{ ms}^{-1}$).

displacement and differential velocity are plotted. The input work is calculated using the histories of applied load and the load point velocity. Specifically, the input work is

$$W = \int_0^t F(\tau)V(\tau)\mathrm{d}\tau \tag{8}$$
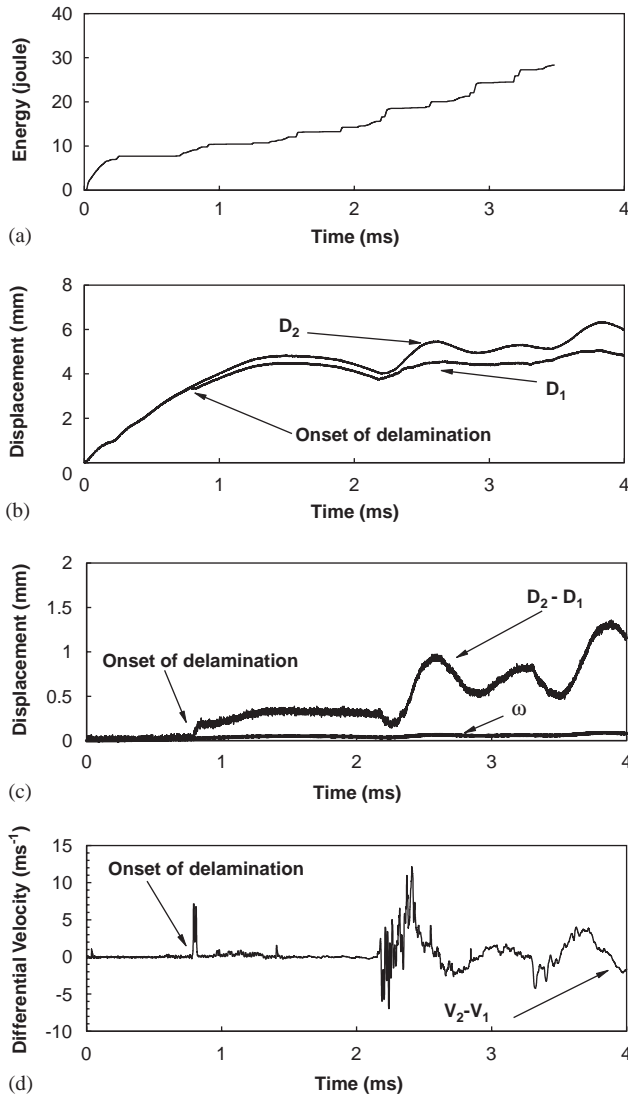
Fig. 8. Histories of input work, displacements, differential displacement and differential velocity for a mode-I experiment with delamination ($V_0 = 6.7$ ms^{-1}).

with F and V being the load on the specimen and load-point velocity, respectively. The input work increases during the loading pulse, indicating continuously forced deformation.

The results for an experiment with an impact velocity of 6.7 ms^{-1} are shown in Fig. 8. The configuration used is that in Fig. 2(a). The location of measurement is 11.71 mm from the impact site ($L = 11.71$ mm). The differential displacement and
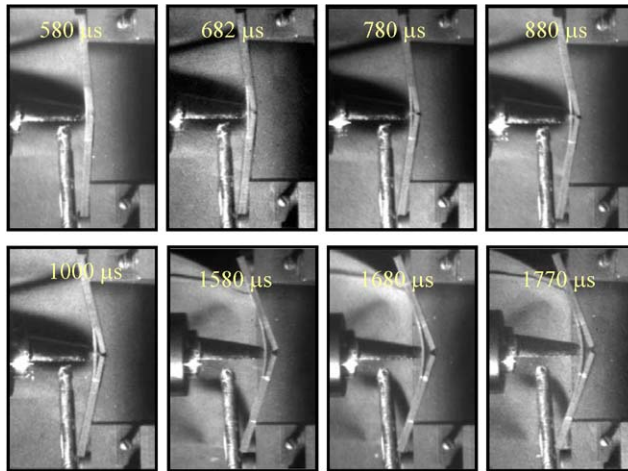
Fig. 9. High-speed photographs showing the deformation in a center crack specimen with $V_0 = 6.7$ ms^{-1}.

velocity profiles show that crack front reaches the point of measurement at 800 μs, when both the differential displacement and differential velocity begin to deviate from zero. A sequence of high-speed digital images recorded for this experiment is shown in Fig. 9. The impactor and a laser probe are visible on the left of the frames. The images show that delamination initiates between 580–682 μs and that the crack front reaches the point of measurement between 780–880 μs providing visual confirmation of what the interferometer measurements indicate. The differential displacement also provides an approximate measure for the interfacial opening displacement. The results show that the interfacial separation is on the order of 1 mm and oscillates under the conditions of the experiment.

An analysis of the effect of specimen rotation on the differential displacement measurement is carried out for the experiment in Fig. 8. An upper bound for the contribution to the differential displacement by rigid body rotation is estimated according to Eqs. (4) and (5). The result is shown in Fig. 8(c). Clearly, this contribution is small and increases gradually from 0 to 0.1 mm. In addition, it has no appreciable effect on the determination of the arrival of the crack front at the location of measurement since it varies slowly and smoothly with time. Note that the onset of delamination is associated with an abrupt upturn of the differential displacement.

At the time of the onset of delamination, 9.3 J of mechanical work has been imparted to the specimen. The absolute displacement of the surfaces is 3.2 mm at the point of measurement. At approximately 1.4 ms, the specimen surfaces attain a local maximum displacement. Subsequent deformation shows oscillations of displacement partly associated with the structural vibrations of the specimen under dynamic loading.

The result of an experiment with two-point measurement of displacements and velocities for crack speed analysis is shown in Fig. 10. The impact velocity is 8.0 ms^{-1} and the opening mode specimen in Fig. 2(a) is used. The histories of displacements
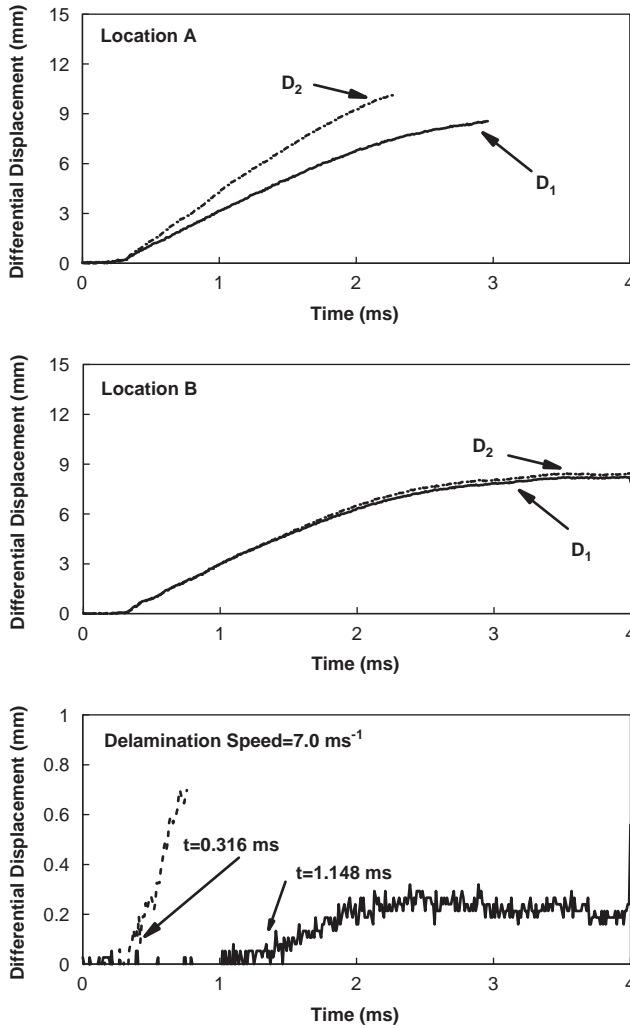
Fig. 10. Two-point measurement of the propagation of interfacial crack in an opening mode specimen, $V_0 = 8.0 \text{ ms}^{-1}$.

and differential displacements at the two locations are shown. Location B is 5.8 mm from location A which is closer to the starter crack or the site of impact. The onset of delamination is 0.316 ms at location A and 1.148 ms at location B, yielding an average crack speed of 7.0 ms^{-1} between these two points.

3.2. Computational validation and analysis of method

The method for detection of fracture used here depends on the opening displacement across crack surfaces which manifest through the differential displacement and velocity

at specimen surfaces. For pure mode-I or mode-I dominated loading conditions, this method works in a straightforward manner. For pure mode-II loading without a component of opening mode of loading, the method described here would not be applicable since there would be no significant normal crack opening displacement for the detectors to measure. Having pointed this out, it is noted that neither configuration in Fig. 2 involves pure mode-II loading. For the opening mode of loading in Fig. 2(a), the applicability of the method used here is obvious: fracture initiation is directly associated with crack tip surface separation. The only question that remains is "do the laser interferometers detect crack initiation right when fracture occurs at the location of measurement since the laser interferometers are sensitive to displacements larger than 4.8 μm and velocities higher than 5.0 $(\mu m)s^{-1}$?". For the primarily shear mode of loading in Fig. 2(b), crack-plane sliding dominates and there may or may not be a significant opening displacement component to allow the method to work. Even when a significant opening component is present, a question exists as to whether the opening component occurs early enough at the propagating shear crack tip to allow a valid determination of delamination time such that vibrometers are not measuring just the subsequent opening of already formed shear crack surfaces. Further complicating the issue is the fact that, for the configuration in Fig. 2(a), discrete matrix cracks at 45° precede interfacial separation and cause delamination when they reach the interlaminar interfaces. It is possible that there may not be a single propagating (mode-II) crack tip for the shear mode specimen in Fig. 2(b). The questions that arise are then: (1) does this configuration induce a significant component of mode-I loading such that the crack surface opening as measured by the interferometers closely follow the actual damage and failure in the specimen?; and (2) what type of failure behavior do the laser interferometers detect?

To answer the above three questions, finite element simulations that provide explicit account of the fracture processes, material layered structure, and dynamic loading are carried out. The cohesive finite element method (CFEM) developed by Minnaar and Zhou (2004) is used to obtain the displacement histories and compare them with actual crack positions. Details of the CFEM model, numerical approach, material characterization and material parameters are provided in the above reference. The conditions analyzed are primarily mode-I, mixed-mode, and primarily mode-II. The configurations analyzed involve a center crack model (primarily mode-I, Fig. 2(a)), shear crack model (mixed-mode with primary mode-II loading, Fig. 2(b)), and an end-notched flexure (ENF) specimen (primarily mode-II, not an actual configuration in our experiments, see Guo and Sun, 1998; Schon, 2000; Schon et al., 2000; Tsai et al., 2001). The ENF specimen has exactly the same size, shape, and layup as that in Fig. 2(a), except that it does not have the starter crack in the middle of the specimen and instead has a 7 mm horizontal pre-crack in the middle of the 90° ply at the left end. In all three cases, a constant velocity is specified at the center of the specimens which have a [0/90/0] layered structure. The center crack specimen has a pre-crack in the lower longitudinal ply that starts at the surface and ends at the interface between the lower longitudinal ply and the transverse ply. In the case of the ENF specimen, a pre-crack exists at the left end of the middle layer. There are no pre-cracks in the shear crack model. The boundary and loading conditions cause the pre-cracks to grow
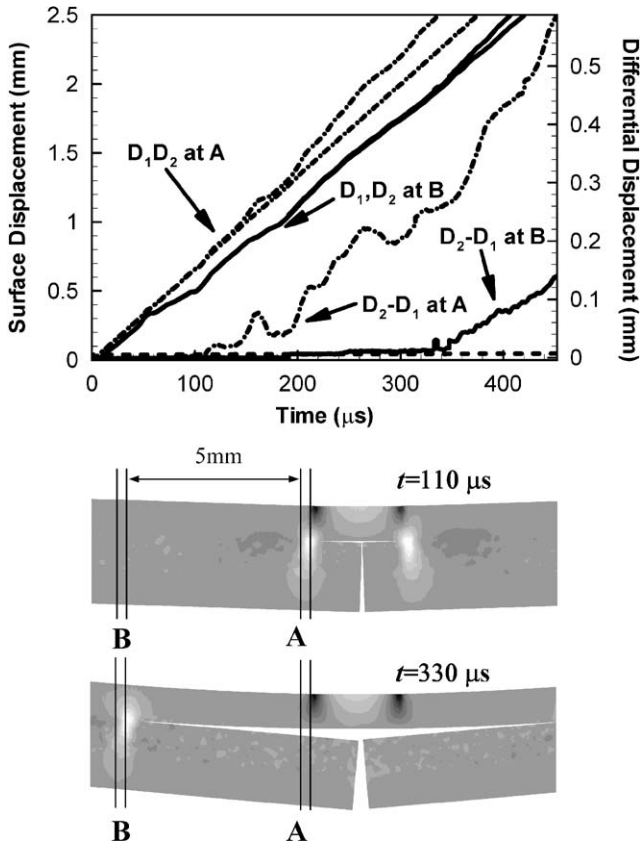
Fig. 11. Numerically predicted progression of delamination and corresponding differential and surface displacements at two measurement locations for the center crack configuration ($V_0 = 6.7$ ms^{-1}), contours denote the distribution of σ_{22}.

towards the upper interlaminar interface in both the center crack and ENF specimens. Matrix cracks form in the middle 90° layer in the shear crack model, propagate toward the upper and lower ply interfaces, and cause delamination along the interfaces.

The simulations mimic the experiments in that the differential displacements of two measurement positions (A and B) corresponding to those in the experiments are recorded. In Fig. 11, the calculated histories of differential displacements and surface displacements in the center crack model are shown by a horizontal dash line. For a perspective on what the readings from the laser interferometers may look like, the threshold (sensitivity) level of the interferometers (4.8 μm) is also shown. The deformed shapes of the region around the interfacial crack of the specimen at two different times (110 and 330 μs) are shown along with the histories of the displacements. The contours of grey indicate the variation of the stress component in the y-direction (σ_{22}). Each measurement beam is denoted by two vertical lines, outlining the finite size of the laser

beam which is focused at that location of the specimen. At approximately $t = 110$ µs, the magnitude of the differential displacement at A reaches the threshold of the inter-ferometers, indicating the approximate time at which delamination would be detected at that location by the interferometers. On the other hand, the stress contours at this time show that the lobe of high stress concentration around the crack tip is at location A, suggesting that the crack front intersects the measurement line at this location at the time indicated by the displacement profiles. The differential displacement at point A increases as the delamination propagates towards point B. The crack front intersects the measurement line at B at approximately 330 µs which is also the time when the differential displacement at B reaches the interferometer threshold. To summarize, the calculation shows that interfacial fracture in the mode I loading of Fig. 2(a) is quite well captured by the laser interferometers. Consequently, the time difference of fracture detection between A and B can be used to obtain the average interfacial crack speed between these two locations in an experiment.

   The calculated results for the shear mode specimen in Fig. 2(b) are shown in Fig. 12. The deformed configurations and the contours of σ_{12} show the advancing delamination front preceded and driven by multiple, distributed 45° matrix cracks that grow towards the ply interfaces. The matrix cracks cause delamination at the points where they intersect the ply interfaces with the intersection at the lower interface occurring first. The differential displacement at A reaches the interferometer sensitivity threshold at approximately $t = 484$ µs. The corresponding stress contours show multiple 45° matrix cracks intersecting the lower interface near A. No clear separation along the lower interface itself is visible between the matrix cracks that have formed ahead of the delamination which is visible to the right of point A. The results for $t = 487$ µs when the differential displacement at B reaches the interferometer sensitivity threshold are similar, with a matrix crack intersecting the lower interplay interface. Clearly, damage and failure in the shear crack specimen occurs primarily through the formation of discrete 45° matrix cracks and normal separation along the interplay interfaces clearly trails behind the formation of matrix cracks. It is reasonable to conclude that the differential displacements measured by the laser interferometers at both A and B are primarily the contributions of the 45° matrix cracks, not those of interfacial separation. Partly because these matrix cracks are not perpendicular to the laser beams, the differential displacements do not indicate the initiation of matrix crack formation *exactly* at A or B. Therefore, the differential displacements are only *approximate* indications of the *onset of damage in the middle ply* near the locations of measurement. In Fig. 12, damage occurs at or near A and B at approximately 484 and 487 µs, respectively. Although later in Fig. 18 experimental measurements at A and B for shear mode specimens will be used to calculate a "delamination speed" for relative comparison with the results for the opening mode specimens. The speed so cited should be regarded as an approximate measure for the rate of lateral progression of damage in the specimen, not as a measure for the speed of an interfacial crack.

   The calculated results for the ENF specimen are shown in Fig. 13. The histories of displacements at A and B and the deformed shapes of the region around the interfacial crack in the specimen at four different times are also shown. The crack front intersects the measurement line at location A at approximately 674 µs, as indicated by the lobe
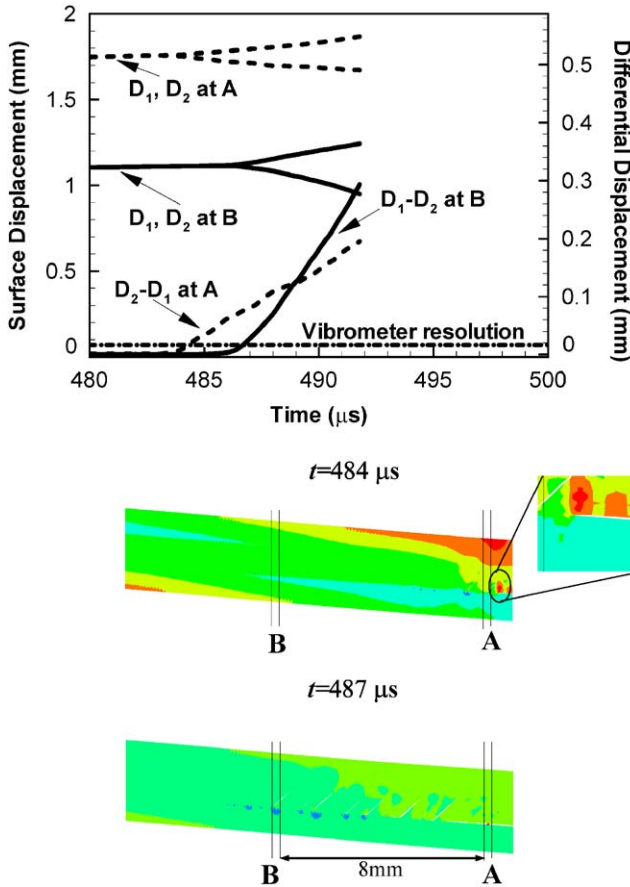
Fig. 12. Numerically predicted progression of matrix cracking/delamination and corresponding differential and surface displacements at two measurement locations for the shear crack configuration ($V_0 = 4.6$ ms^{-1}); contours denote the distribution of σ_{12}.

of the contours of σ_{12}. At this time, the magnitude of the differential displacement is below the detection threshold of the interferometers. The differential displacement at point A increases as the delamination propagates towards point B and the magnitude of the differential displacement at A reaches the threshold at 675 μs, resulting in a delay in detection of approximately 1 μs. At 675 μs, the crack tip is approximately 0.6 mm past point A. This distance is the spatial delay in crack detection at A. Similarly, the delay in detection at point B is approximately 2 μs (680 μs vs. 678 μs) in time and 0.5 mm in space. The delays are due to the detector sensitivity and due to the smaller opening displacements associated with the primarily shear mode of loading in this specimen configuration. Note that, if the interferometers had a sensitivity of 0 μm, crack arrivals at A and B would almost instantaneously be reflected in the differential displacement profiles. Obviously, the measurement error for the ENF specimen is larger than the
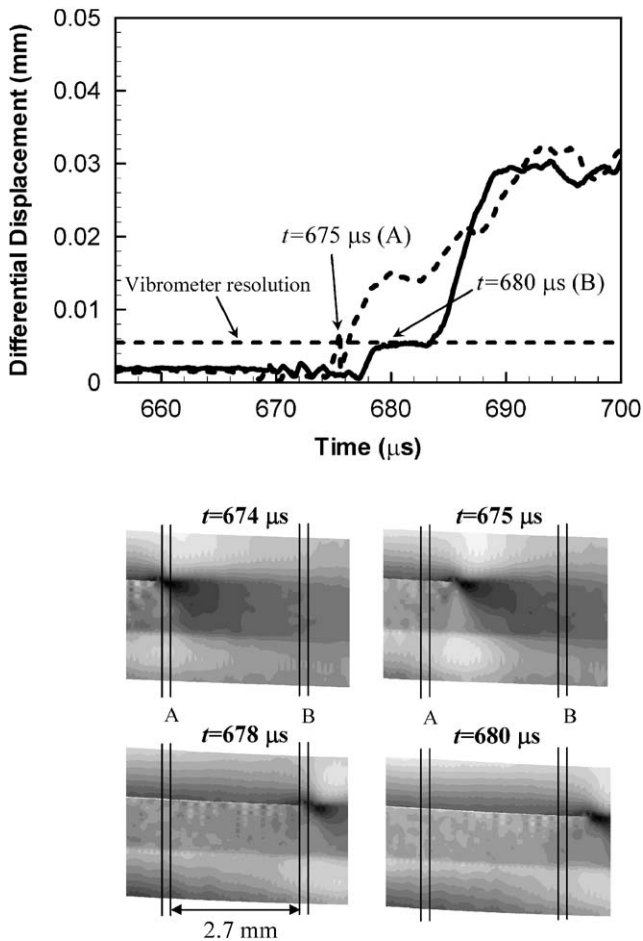
Fig. 13. Numerically predicted progression of delamination and corresponding differential displacements at two measurement locations for the ENF shear configuration ($V_0 = 5$ ms^{-1}), contours denote the distribution of σ_{12}.

error for the opening mode specimen. Whether this level of error is acceptable or not depends on the circumstances of an analysis. The result obtained here would support the use of the experimental method for the ENF specimen configuration, if the delays seen here are regarded as acceptable for a particular problem.

The possibility of crack detection through normal differential displacements for the above three specimen configurations depends on an appreciable opening component present during the fracture process. The simulations show that this is true even for the shear and ENF specimens. The conclusion here does not automatically justify the use of our method under conditions not analyzed here. Analyses are needed for other situations with primarily shear conditions.
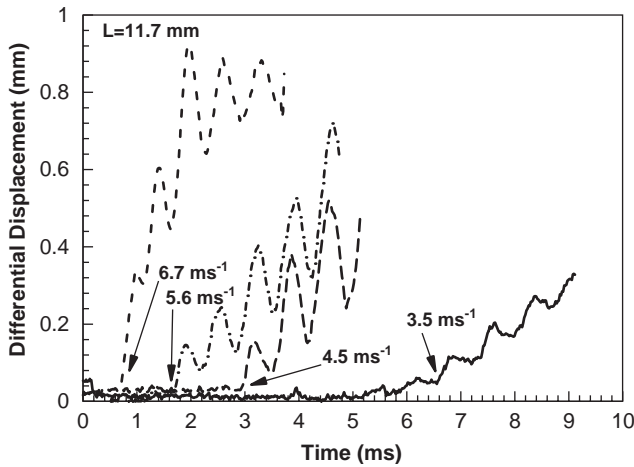
Fig. 14. Onset and progression of delamination at different impact velocities (opening mode specimen).

3.3. Effect of loading rate

Initially, only two interferometers were available and, therefore, only one-point measurements were made. The speed of delamination was estimated from the one-point measurements, using results from different specimens with identical loading conditions. Specifically, the locations of the interferometers along the span of the specimens are varied between experiments. The time for the onset of delamination is recorded in each case and the difference in the times is used to calculate the average speed of the interfacial crack front. For the center crack specimen configuration, this estimate is more accurate, since delamination always initiates at nearly identical times from the location of the pre-crack. The results are repeatable for various boundary and load conditions. This is not the case for the shear crack specimen, however. The analysis assumes that matrix cracking/delamination initiates at the same location and the same time and progresses in the same manner in all specimens. It was quickly realized that one-point measurements are insufficient to obtain repeatable results for the shear configuration. The reason is that the location and time of the initial matrix crack vary among experiments due to local changes in the fiber volume fraction (Fig. 1) and due to other experimental factors. The simultaneous use of four interferometer systems focused on two locations eliminates the above issue. Such a setup obviates the need to know the specific time and location of damage initiation. The difference between the times of crack detection at the measurement points and the distance between them directly yield the average crack speed. Results of the one-point measurements are discussed first, followed by discussions of the results obtained using the two-point setup.

Experiments are conducted at impact velocities of 3.5, 4.5, 5.6 and 6.7 ms^{-1} to analyze the effect of loading rate on interlayer fracture. We first focus on results from the opening mode specimens.

Fig. 14 shows a summary of the histories of the differential displacement at different impact velocities at a distance of $L = 11.71$ mm from the center of the specimen. The
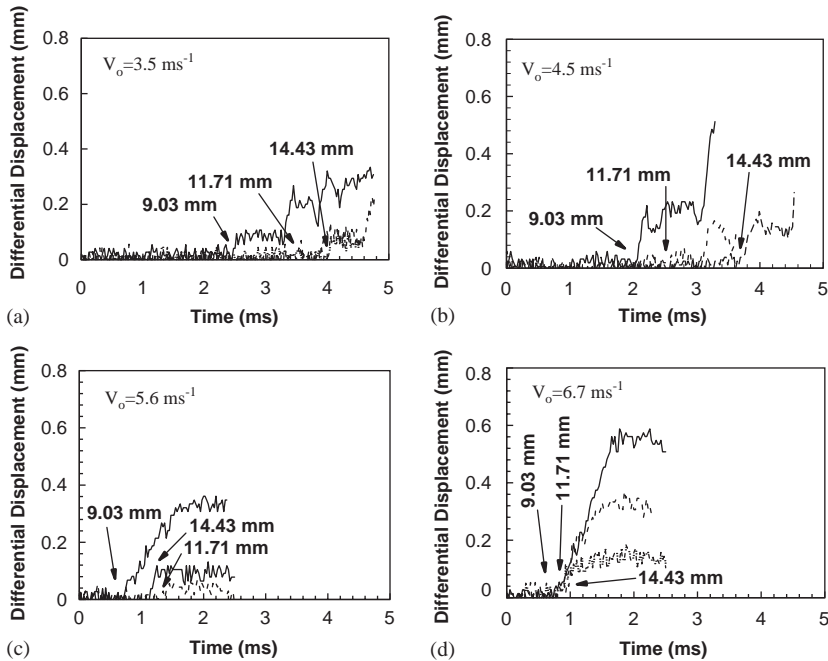
Fig. 15. Detection of delamination front at different locations (opening mode specimen).

time of crack detection decreases from 5.6 to 0.6 ms as the impact velocity is increased from 3.5 to 6.7 ms^{-1}. Note the stress wave speeds in Table 1. In particular, it takes 23 μs for the shear wave to propagate from the center to the end of the specimen and 16 μs for the dilatational wave (perpendicular to the fibers) to reach the end of the specimen. At the time of detection, the (slower) shear wave has completed 12 reverberations between the center and the end of the specimen. Therefore, the process here is not only driven by dynamic effects alone. The process is also affected by layered material structure, support conditions and specimen size scale.

Multiple experiments with the same impact velocity are performed, allowing measurements to be taken at different locations under the same conditions. Fig. 15 shows the results of these experiments, for four different levels of impact velocity. The average speed of delamination between the locations of measurement is calculated. The calculation uses the difference in the times of detection and the distance between the measurement points. The results are plotted in Fig. 16. The average speed calculated between $L = 9.03$ and 11.71 mm is between 3 and 13 ms^{-1}. No clear trend is discernable in the speed as the impact velocity is increased from 3.5 to 6.7 ms^{-1}. The average crack speed between $L = 11.7$ and 14.43 mm varies between 2 and 33 ms^{-1}, depending on impact velocity. It appears that the speed of delamination increases as the impact velocity is increased from 3.5 to 6.7 ms^{-1}, with the exception of the case with an impact velocity of 4.5 ms^{-1} (which has a crack speed of 2 ms^{-1}). We note that the estimate of crack speed using results from multiple specimens carries higher
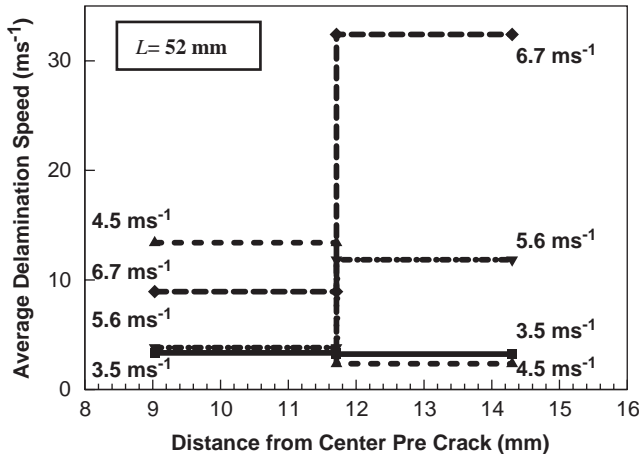
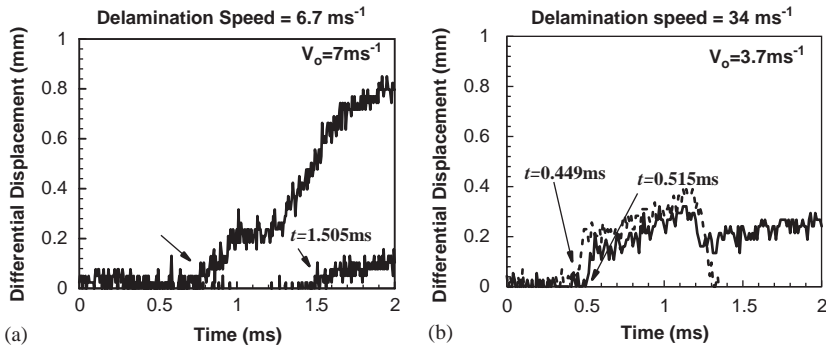Fig. 16. Average delamination speed at various impact velocities (opening mode).

Fig. 17. Two-point measurement of onset and progression of delamination/damage, (a) center crack configuration ($V_0 = 7.0$ ms^{-1}), (b) shear crack configuration ($V_0 = 3.7$ ms^{-1}).

levels of errors. Firstly, there is a slight variation in impact velocity among experiments intended to have exactly the same loading conditions. Secondly, the material inhomogeneity seen in Fig. 1 causes small variations in response among specimens. Thirdly, variance in the width and depth of the starter crack can also lead to variations in behavior among different specimens. The influence of these factors on crack speed measurement can be avoided by calculating the speed of delamination from two-point measurements made simultaneously during a single impact event on a single specimen.

Fig. 17(a) shows the histories of the differential displacements at two measurement locations for a specimen with an impact velocity of 7.0 ms^{-1}. The distance between the two points is 5.6 mm. Delamination is observed at $t = 0.316$ ms at A and $t = 1.148$ ms at B, giving rise to a crack propagation time of 0.832 ms and an average crack speed of 6.7 ms^{-1} between the two locations. The results of experiments with a range of impact
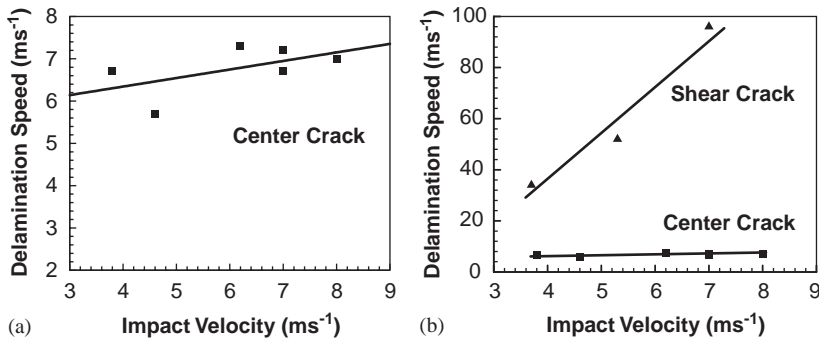
Fig. 18. Effect of impact velocity on delamination/damage propagation speed, (a) opening mode, (b) comparison of opening and shear modes.

velocities are summarized in Fig. 18(a). A slight increase of crack speed with impact velocity is seen. The rate of increase is approximately 0.2 ms^{-1} for every 1 ms^{-1} increase in impact velocity. This is somewhat expected since the loading rate is low and the time scale of the fracture event is much longer than the time it takes for the longitudinal and shear stress waves to propagate to the specimen boundaries. Also, it is noted that the delamination speed is small compared with the speeds of stress waves.

Two-point measurements are also used to analyze the influence of impact velocity on damage propagation speed under primarily shear modes of loading. Recall that the damage and failure for this specimen configuration does not involve a single, well-defined interfacial delamination front and that the progression of damage along the specimen involves multiple matrix cracks. The propagation of damage analyzed here can only be interpreted in an approximate, averaged sense. Fig. 17(b) shows the histories of the differential displacements at two locations along the span of a specimen with the configuration in Fig. 2(b). The average speed of damage progression measured between the measurement points is 34 ms^{-1} at an impact velocity of 3.7 ms^{-1}. The speeds at other loading rates are summarized in Fig. 18(b). There is a significant increase of this speed with loading rate. A comparison of the speeds of delamination propagation for opening cracks and the speeds of damage propagation for shear cracks is given in Fig. 18(b) as well. The speeds for the mode-II specimen are significantly higher and more loading rate sensitive than the speeds for opening cracks. This observation is consistent with the results of higher crack speeds in mode II reported by Huang et al. (1998, 1999).

4. Summary and discussion

A novel technique for time-resolved analyses of interfacial fracture in layered materials has been developed. The technique uses laser interferometers to record surface

displacements and velocities. The analyses of interfacial fracture involve the deduction of normal crack face separations as a function of time. Measurements at multiple locations are used to obtain average crack speeds between the measurement points. Experiments and numerical calculations show that, for primarily opening mode of loading, this technique provides a reliable and sensitive means for quantifying the time history of fracture progression along an interface, time history of crack face opening displacement, and crack speed. The analyses show that this technique also provides a useful measure for identifying the approximate times for the onset of damage at different locations in the shear crack specimen and for approximate characterization of the interfacial delamination speeds in the ENF specimen. Experiments have provided quantification of interlaminar crack speeds (opening mode specimen) and the damage propagation speeds (shear mode specimen) in layered composites under conditions of low velocity, transverse impact loading. The crack and failure propagation speeds are between 5 and 100 ms^{-1}, much lower than those reported by Lambros and Rosakis (1995, 1997a,b) and Rosakis et al. (1999). Opening cracks propagate at relatively lower speeds. Higher damage propagation speeds are observed under primarily shear modes of loading. In addition, a significantly stronger dependence of speeds on loading rate is found under primarily mode-II conditions. It is important to point out that, since the current method uses normal displacements for failure identification, it is unsuitable for situations involving pure mode-II loading without an appreciable opening mode of deformation. The results and conclusions presented here are specific to the three experimental configurations (two of which are actually used in the experiments, one has been used in the literature but is not used in the experiments of this paper). The applicability of this technique to other configurations not discussed here should be specifically analyzed. As a possible further extension of this technique, laser interferometers that measure transverse (in-plane) displacements and transverse velocities can be used to analyze the initiation and propagation of cracks under purely mode-II conditions. Such interferometers are indeed available and could provide an improvement of the technique introduced here.

The method developed here offers many advantages over other experimental techniques. The technique allows time-resolved tracking of the onset and progression of delamination and/or damage throughout the course of an experiment. It also allows measurement of interlayer crack speeds. The technique is optical and non-contact in nature, allowing measurements to be taken away from the specimen. Therefore, no perturbation of the deformation being measured occurs. The high temporal responses of the laser interferometers and the digital instrumentation ensure time resolutions unavailable in other experimental approaches. The system described here includes a complete set of diagnostics for measurement of histories of load, deformation, and input work. The technique focuses on delamination along interfaces and matrix cracking in layered systems and allow their effects of be quantified. It is worthwhile to point out that the laser interferometers and optical fiber heads here can be used even for diffuse surfaces with poor optical characteristics and tolerate specimen surface rotations. Unlike Moire-interferometers (Lagace and Wolf, 1993) and the CGS system (Lambros and Rosakis, 1997a), optically flat surfaces and high surface reflectivity are not required.

Acknowledgements

References

Abrate, S., 1991. Impact on laminated composite materials. Appl. Mech. Rev. 44 (4), 155–190.

Abrate, S., 1994. Impact on laminated composites: recent advances. Appl. Mech. Rev. 47, 517–544.

Abrate, S., 1998. Impact on Composite Structures. Cambridge University Press, Cambridge.

Abry, J.C., Bochard, S., Chateauminois, A., Salvia, M., Giraud, G., 1999. In situ detection of damage in CFRP laminates by electrical resistance measurements. Compos. Sci. Technol. 59 (6), 925–935.

Abry, J.C., Choi, Y.K., Chateauminois, A., Dalloz, B., Giraud, G., Salvia, M., 2001. In-situ monitoring of damage in CFRP laminates by means of AC and DC measurements. Compos. Sci. Technol. 61 (6), 855–864.

Agarwal, B.D., Broutman, L.J., 1990. Analysis and Performance of Fiber Composites. Wiley, New York.

Benmedakhene, S., Kenane, M., Benzeggagh, M.L., 1999. Initiation and growth of delamination in glass/epoxy composites subjected to static and dynamic loading by acoustic emission monitoring. Compos. Sci. Technol. 59 (2), 201–208.

Cantwell, W.J., Morton, J., 1991. The impact resistance of composite materials—a review. Composites 22 (5), 347–361.

Cartie, D.D.R., Irving, P.E., 2002. Effect of resin and fiber properties on impact and compression after impact performance of CFRP. Compos. Part A: Appl. Sci. Manuf. 33 (4), 483–493.

Chai, H., Knauss, W.G., Babcock, C.D., 1983. Observation of damage growth in compressively loaded laminates. Exp. Mech. 23 (3), 329–337.

Chang, F.K., Lessard, L.B., 1991. Damage tolerance of laminated composites containing an open hole and subjected to compressive loading: part I—Analysis. J. Compos. Mater. 25, 2–43.

Chang, F.K., Choi, H.Y., Jeng, S.T., 1989. Characterization of impact damage in laminated composites. Proceedings of the 34th International SAMPE Symposium, Reno, NV, pp. 702–713.

Chang, F.K., Choi, H.Y., Jeng, S.T., 1990a. Characterization of impact damage in laminated composites. SAMPE 26 (1), 18–25.

Chang, F.K., Choi, H.Y., Wang, H.S., 1990b. Damage of laminated composites due to low velocity impact. 31st AIAA/ASME/ASCE/AHS/ASC Structures, Structural Dynamics and Material Conference, Long Beach, CA.

Choi, H.Y., Wang, H.S., Chang, F.K., 1990. Effect of laminate configuration on low-velocity impact damage of laminated composites. Proceedings of the 22nd International SAMPE Technical Conference, pp. 484–493.

Choi, H.Y., Downs, R.J., Chang, F.K., 1991a. A new approach toward understanding damage mechanisms and mechanics of laminated composites due to low-velocity impact: part I—experiments. J. Compos. Mater. 25, 992–1011.

Choi, H.Y., Wu, H.-Y.T., Chang, F.-K., 1991b. A new approach toward understanding damage mechanisms and mechanics of laminated composites due to low-velocity impact: part II—analysis. J. Compos. Mater. 25, 1012–1038.

Cristescu, N., Malvern, L.E., Sierakowski, R.L., 1975. Failure mechanisms in composite plates impacted by blunt-ended penetrators. ASTM STP 568, 159–172.

Davies, G.A.O., Zhang, X., 1995. Impact damage prediction in carbon composite structures. Int. J. Impact Eng. 16 (1), 149–170.

Davies, G.A.O., Hitchings, D., Wang, J., 2000. Prediction of threshold impact energy for onset of delamination in quasi-isotropic carbon/epoxy composite laminates under low-velocity impact. Compos. Sci. Technol. 60 (1), 1–7.

Dost, E.F., Ilcewicz, L.B., Avery, W.B., 1991. Effects of stacking sequence on impact damage resistance and residual strength for quasi-isotropic laminates. In: O'Brien, T.K., (Ed.), ASTM STP, pp. 467–500.

Grady, J.E., Sun, C.T., 1986. Dynamic delamination crack propagation in a graphite/epoxy laminate. ASTM STP 907, 5–31.

Guo, C., Sun, C.T., 1998. Dynamic Mode-I crack-propagation in a carbon/epoxy composite. Compos. Sci. Technol. 58 (9), 1405–1410.

Hallett, S.R., 2000. Three-point beam impact test in T300/914 carbon-fibre composites. Compos. Sci. Technol. 60, 115–124.

Huang, Y., Wang, W., Liu, C., Rosakis, A.J., 1998. Intersonic crack growth in bimaterial interfaces: an investigation of crack face contact. J. Mech. Phys. Solids 46 (11), 2233–2259.

Huang, Y., Wang, W., Liu, C., Rosakis, A.J., 1999. Analysis of intersonic crack growth in unidirectional fiber-reinforced composites. J. Mech. Phys. Solids 47, 1893–1916.

Joshi, S.P., Sun, C.T., 1985. Impact induced fracture in a laminated composite. J. Compos. Mater. 19, 51–66.

Joshi, S.P., Sun, C.T., 1986. Impact-induced fracture in quasi-isotropic laminate. J. Compos. Technol. Res. 19, 40–46.

Lagace, P.A., Wolf, E., 1993. Impact damage resistance of several laminated composite systems. 34th AIAA Structures, Structural Dynamics and Materials Conference, La Jolla, CA, pp. 1863–1872.

Lambros, J., Rosakis, A.J., 1995. Dynamic delamination and fracture in thick fiber reinforced composites, high strain rate effects on polymer, metals and ceramic matrix composites and other advanced materials. ASME, AD 48, 97–107.

Lambros, J., Rosakis, A.J., 1997a. Dynamic crack initiation and growth in thick unidirectional graphite/epoxy plates. Compos. Sci. Technol. 57, 55–65.

Lambros, J., Rosakis, A.J., 1997b. Dynamic crack initiation and growth in thick unidirectional graphite/epoxy plates. Compos. Sci. Technol. 57 (1), 55–65.

La Saponara, V., Kardomateas, G.A., 2000. Statistical considerations in the analysis of data from fatigue test on delaminated cross-ply graphite/epoxy composites. J. Eng. Mater. Technol. 122, 409–414.

Liu, S., Kutlu, Z., Chang, F.K., 1993. Matrix cracking and delamination propagation in laminated composites subjected to transversely concentrated loading. J. Compos. Mater. 27 (5), 436–470.

Minnaar, K., Zhou, M., 2004. Numerical simulations of impact-induced delamination in layered composites, to be submitted.

Park, S.W., Zhou, M., 2000. Time-resolved impact response and damage of fiber-reinforced composite laminates. J. Compos. Mater. 34 (10), 879–904.

Pelegri, A.A., Kardomateas, G.A., 1998. Intralayer cracking in delaminated glass/epoxy and graphite/epoxy laminates under cyclic or monotonic loading. 39th AIAA/ASME/ASCE/AHS/ASC Structures, Structural Dynamics, and Materials Conference and Exhibit and AIAA/ASME/AHS adaptive Structures Forum, Long Beach, CA, pp. 1534–1544.

Rosakis, A.J., Samudrala, O., Coker, D., 1999. Cracks faster than the shear wave speed. Science 284, 1337–1340.

Salpekar, S.A., 1993. Analysis of delamination in cross-ply laminates initiating from impact induced matrix cracking. J. Compos. Technol. Res., 88–94.

Schoeppner, G.A., Abrate, S., 2000. Delamination threshold loads for low velocity impact on composite laminates. Compos. Part A: Appl. Sci. Manuf. 31 (9), 903–915.

Schon, J., 2000. Coefficient of friction of composite delamination surfaces. Wear 237 (1), 77–89.

Schon, J., Nyman, T., Blom, A., Ansell, H., 2000. Numerical and experimental investigation of a composite ENF-specimen. Eng. Fract. Mech. 65 (4), 405–433.

Strait, L.H., Karasek, M.L., Amateau, M.F., 1992. Effects of stacking sequence on the impact resistance of carbon fiber reinforced thermoplastic toughened epoxy laminates. J. Compos. Mater. 26 (12), 1725–1740.

Sun, C.T., Manoharan, M.G., 1989. Growth of delamination due to bending in a [905/05/905] laminate. Compos. Sci. Technol. 34, 365–377.

Takeda, N., Sierakowski, R.L., Ross, C.A., Malvern, L.E., 1982. Delamination-crack propagation in ballistically impacted glass/epoxy composite laminates. Exp. Mech. 22 (1), 19–25.

Tao, J., Sun, C.T., 1997. Influence of ply orientation on delamination in composite laminates. J. Compos. Mater. 32, 1933–1947.

Todoroki, A., Tanaka, Y., Shimamura, Y., 2002. Delamination identification of cross-ply graphite/epoxy composite beams using electric resistance change method. Compos. Sci. Technol. 62 (9), 1151–1160.

Tsai, J.L., Guo, C., Sun, C.T., 2001. Dynamic delamination fracture toughness in unidirectional polymeric composites. Compos. Sci. Technol. 61 (1), 87–94.

Wiggenraad, J.F.M., Zhang, X., Davies, G.A.O., 1999. Impact damage prediction and failure analysis of heavily loaded, blade-stiffened composite wing panels. Compos. Struct. 45, 81–103.